

Joint X-ray/neutron structure of *Lentinus similis* AA9_A at room temperature

Tobias Tandrup,^{a,†} Leila Lo Leggio^a and Flora Meilleur^{b,c,*}

^aDepartment of Chemistry, University of Copenhagen, Universitetsparken 5, 2100 Copenhagen, Denmark, ^bDepartment of Molecular and Structural Biochemistry, North Carolina State University, Campus Box 7622, Raleigh, NC 27695, USA, and ^cNeutron Scattering Division, Oak Ridge National Laboratory, PO Box 2008, Oak Ridge, TN 37831, USA.

*Correspondence e-mail: fmeille@ncsu.edu

Received 26 August 2022

Accepted 23 November 2022

Edited by M. J. Romao, Universidade Nova de Lisboa, Portugal

† Current affiliation: Department of Biotechnology and Biomedicine, Technical University of Denmark, Søtofts Plads 224, 2800 Kongens Lyngby, Denmark.

Keywords: lytic polysaccharide mono-oxygenases; *Lentinus similis* AA9_A; copper metalloenzymes; protonation states; neutron crystallography.

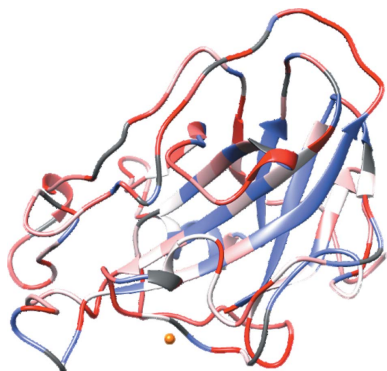
PDB reference: Neutron crystal structure of *Lentinus similis* AA9_A at room temperature, 8e1w

Supporting information: this article has supporting information at journals.iucr.org/f

Lytic polysaccharide mono-oxygenases (LPMOs) are copper metalloenzymes which cleave polysaccharides oxidatively and are important in pathogen biology, carbon cycling and biotechnology. The *Lentinus similis* family AA9 isoform A (*LsAA9_A*) has been extensively studied as a model system because its activity towards smaller soluble saccharide substrates has allowed detailed structural characterization of its interaction with a variety of substrates by X-ray crystallography at high resolution. Here, the joint X-ray/neutron room-temperature crystallographic structure of carbohydrate-free *LsAA9_A* in the copper(II) resting state refined against X-ray and neutron data at 2.1 and 2.8 Å resolution, respectively, is presented. The results provide an experimental determination of the protonation states of the copper(II)-coordinating residues and second-shell residues in *LsAA9_A*, paving the way for future neutron crystallographic studies of LPMO–carbohydrate complexes.

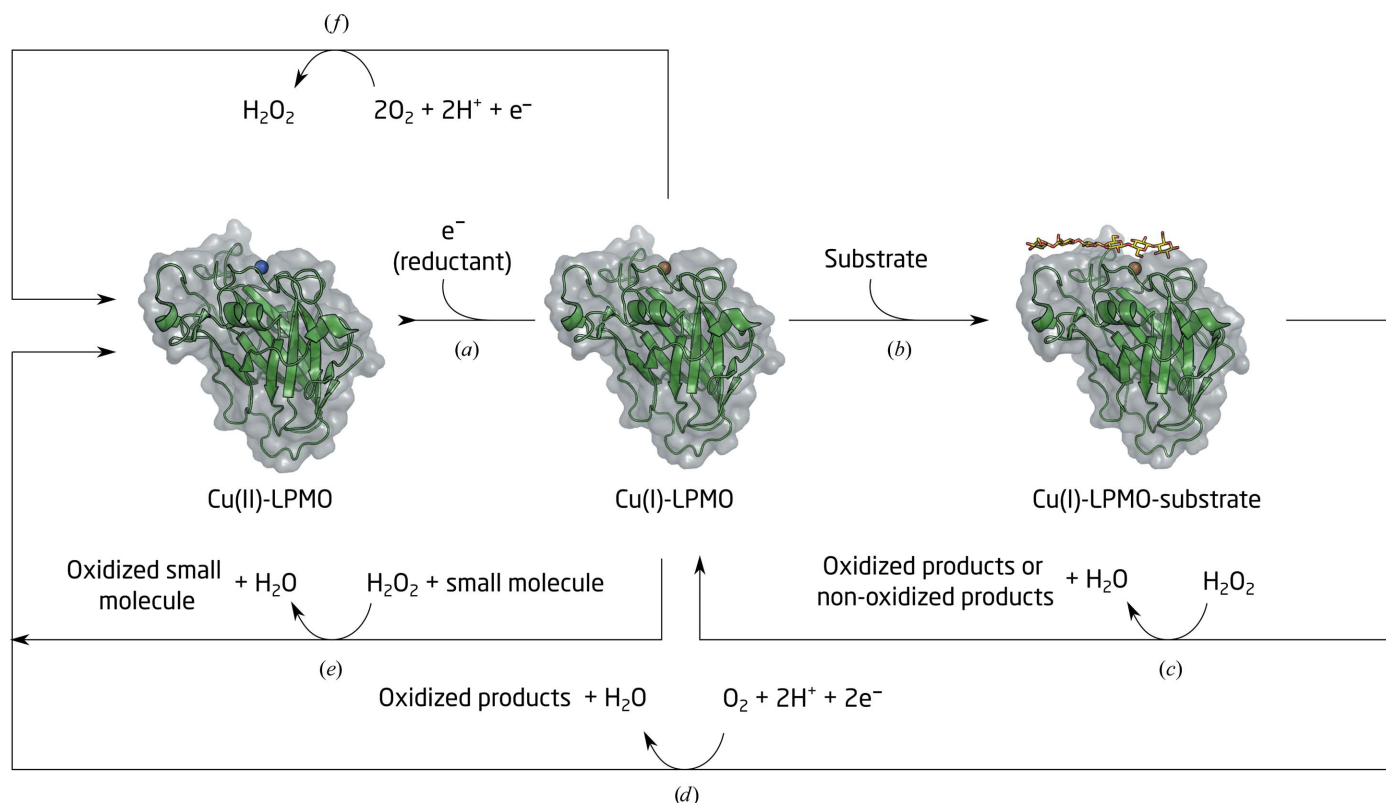
1. Introduction

Copper-containing lytic polysaccharide mono-oxygenases (LPMOs) are a class of metalloenzymes that have recently been brought to the forefront of research advancing renewable energy and the conversion of biomass to value-added chemicals (Johansen, 2016), as well as having increasingly recognized biological functions in pathogenesis (Vandhana *et al.*, 2022). They are classified as auxiliary activities (AA) families AA9–AA11 and AA13–AA17 in the Carbohydrate Active enZymes (CAZy) database (Levasseur *et al.*, 2013; Drula *et al.*, 2022). Fungal LPMOs are some of many enzymes secreted by fungi to break down plant matter, namely cellulose, and release glucose. LPMOs randomly oxidize recalcitrant crystalline cellulose, disrupting local crystallinity and creating new cellobextrin chain ends that serve as additional starting points for the endo- and exo-activities of glycoside hydrolases (GHs; Agger *et al.*, 2014). While LPMOs were first described as mono-oxygenases, binding molecular dioxygen as a co-substrate, it is now established that LPMOs also have peroxidase/peroxygenase activity (Bissaro *et al.*, 2017). The mono-oxygenase reaction requires molecular oxygen, two protons and two single-electron transfers from either small-molecule reductants or electron-donating proteins such as cellobiose dehydrogenases that are co-secreted by fungi (Fig. 1). Mechanistic details, including the source of protons and the chemical nature of oxygen-activated reaction intermediates, for both the O₂-based and H₂O₂-based mechanisms remain to be elucidated in order to understand how these enzymes carry out carbohydrate oxidation.



OPEN ACCESS

Published under a CC BY 4.0 licence


Figure 1

LPMO reaction scheme. Depending on the specific LPMO and the available conditions, one of several reactions may take place. Initial reduction (a) and substrate binding (b) is followed by the formation of oxidized or non-oxidized chain ends depending on the specific LPMO, using H₂O₂ (c) or O₂ (d) as a co-substrate. Oxidizing reactions may also occur in the presence of small molecules (e). In the presence of O₂ but without substrate, the LPMO may produce H₂O₂ (f).

Neutron protein crystallography is a powerful tool for investigating protein chemistry because it directly locates H-atom positions in a protein structure (Schröder *et al.*, 2018). Early X-ray and neutron crystallographic studies of LPMOs from the AA9 family have focused on understanding the activation of O₂ by *Neurospora crassa* LPMO 9D (*NcAA9_D*) in the absence of substrate (Bodenheimer *et al.*, 2017; O'Dell, Swartz *et al.*, 2017; O'Dell, Agarwal *et al.*, 2017; Schröder *et al.*, 2021, 2022). In addition to the direct determination of protonation states, these structures have revealed the geometry and the chemical nature of the initial Cu–O₂⁻ and Cu–O₂H intermediates. These results are important to understand the activation of O₂ (Fig. 1f). However, elucidation of the mechanism of carbohydrate oxidation requires the trapping of early intermediates in an LPMO–carbohydrate complex (Fig. 1b). The insolubility of the substrates of *NcAA9_D* has so far prevented the investigation of LPMO–O₂–carbohydrate complexes. Later, *LsAA9_A* was demonstrated to be active towards soluble oligosaccharides and the first structures of an LPMO enzyme in complex with short soluble carbohydrates were reported (Frandsen *et al.*, 2016; Simmons *et al.*, 2017). *LsAA9_A* has now been used extensively as a model LPMO, including high-resolution crystallographic studies to determine the protonation state of key histidine residues (Banerjee *et al.*, 2022) and detailed photo-reduction studies (Tandrup *et al.*, 2022). Furthermore, the dependence of *LsAA9_A* on H₂O₂ has been established and a

novel twist on the LPMO mechanism has been suggested, at least for this specific enzyme (Brander *et al.*, 2021). Therefore, *LsAA9_A* opens the opportunity to analyze substrate-bound enzyme complexes and the activation of H₂O₂ using neutron crystallography.

Here, we report the neutron structure of carbohydrate-free *LsAA9_A* in the copper(II) resting state. The protonation states of catalytic residues at and around the copper center are determined.

2. Materials and methods

2.1. Protein purification and crystal growth

The fungal enzyme *LsAA9_A* was expressed in *Aspergillus oryzae*, purified and deglycosylated with endoglycosidase H as described previously (Frandsen *et al.*, 2016; Simmons *et al.*, 2017; Tandrup *et al.*, 2020). The protein sample was pre-incubated with an equimolar amount of copper(II) acetate for 1 h at 4°C prior to crystallization setup. Crystals of *LsAA9_A* were grown via sitting-drop vapor diffusion by adapting previously reported protocols (Frandsen *et al.*, 2016). For neutron crystallography, crystals were grown in a nine-well glass-plate and sandwich-box setup (Hampton Research) at 10°C. The sitting drops were equilibrated against 50 ml reservoir solution consisting of 3.0 M NaCl, 0.1 M citric acid pH 3.5. Large crystals grew from 100 µl sitting drops prepared

at a protein concentration ranging from 16 to 20 mg ml⁻¹ in 1.3 M NaCl, 0.1 M citric acid pH 3.5 (Fig. 2).

2.2. Neutron and X-ray data collection at room temperature

Crystals were mounted in thin-walled quartz capillaries (Hampton Research) using hydrogenated crystallization buffer at pH 3.5 from the sandwich box. Excess buffer was removed and plugs of 100 mM deuterated citric acid buffer at pD 5.5 (pH electrode reading 5.1) containing 3 M NaCl were placed on both sides of the crystal prior to sealing the capillaries to vapor-exchange the crystal solvent water molecules and labile protein H atoms to D₂O molecules and D atoms, respectively. The pH was increased from 3.5 to 5.5 to prevent disorder of the histidine brace (Frandsen *et al.*, 2017). The exchange occurred over two weeks prior to neutron data collection.

Neutron time-of-flight diffraction data were collected at room temperature on the MaNDi instrument at the Spallation Neutron Source (Coates & Sullivan, 2020; Meilleur *et al.*, 2018). An incident neutron wavelength bandpass of 3–5 Å was used. A total of six diffraction patterns with a $\Delta\phi$ of 10° between frames were collected with an exposure of 48 h per frame. Following neutron diffraction data collection, an X-ray data set was collected from the same crystal at room temperature on a microfocus rotating-anode X-ray diffractometer (MicroMax-007 HF, Rigaku). A total of 57 diffraction patterns were collected with a $\Delta\phi$ of 1.0° and an exposure of 45 s per frame.

The neutron data set was reduced using the *Mantid* package (Arnold *et al.*, 2014) and integrated using three-dimensional profile fitting (Sullivan *et al.*, 2018). The data were wavelength-normalized using *LAUENORM* from the *LAUEGEN* suite (Helliwell *et al.*, 1989; Campbell *et al.*, 1998; Arzt *et al.*, 1996). The X-ray data were indexed and integrated using *CrysAlis^{Pro}* (Rigaku, Woodlands, Texas, USA) and scaled and merged with *AIMLESS* in the *CCP4* suite (Evans & Murshudov, 2013; Winn *et al.*, 2011). Data-collection and processing statistics are summarized in Table 1. The data and structure have been deposited in the Protein Data Bank (PDB entry 8e1w; Berman *et al.*, 2000).

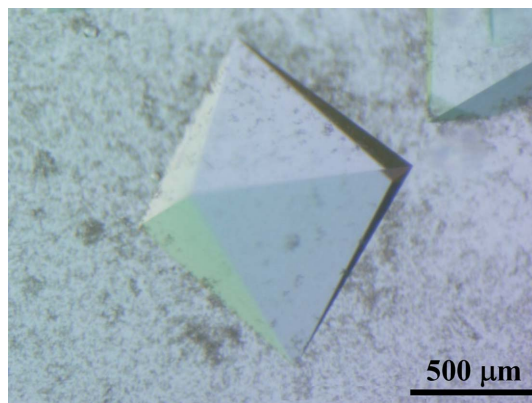


Figure 2
Octahedral crystal of hydrogenated *LsAA9_A* grown from 100 μ l sitting drops.

Table 1
Neutron and X-ray data-collection and joint refinement statistics.

Values in parentheses are for the highest resolution shell.

	X-ray	Neutron
Wavelength (Å)	1.54	3.0–5.0
Resolution range (Å)	30.67–2.10 (2.18–2.10)	14.8–2.80 (2.90–2.80)
Space group	<i>P</i> 4 ₁ 32	<i>P</i> 4 ₁ 32
<i>a</i> , <i>b</i> , <i>c</i> (Å)	126.469, 126.469, 126.469	126.469, 126.469, 126.469
α , β , γ (°)	90, 90, 90	90, 90, 90
Total reflections	212841 (21125)	91012 (7436)
Unique reflections	20749 (2019)	8942 (869)
Multiplicity	10.3 (10.5)	10.2 (8.6)
Completeness (%)	99.87 (99.95)	99.3 (99.9)
Mean <i>I</i> / σ (<i>I</i>)	14.16 (2.09)	10.1 (4.8)
<i>R</i> _{merge}	0.1758 (1.482)	0.262 (0.290)
<i>R</i> _{meas}	0.1851 (1.559)	0.275 (0.308)
<i>R</i> _{p.i.m.}	0.0571 (0.4802)	0.081 (0.102)
CC _{1/2}	0.988 (0.746)	0.920 (0.348)
Reflections used in refinement	20738	8850
Reflections used for <i>R</i> _{free}	1033	886
<i>R</i> _{work}	0.1484	0.2251
<i>R</i> _{free}	0.1702	0.2598
No. of non-H atoms		
Total		1931
Macromolecule		1798
Cu		1
Cl		1
<i>N</i> -Acetylglucosamine		14
Solvent		117
Protein residues		235
R.m.s.d., bond lengths (Å)		0.015
R.m.s.d., angles (°)		1.27
Ramachandran favored (%)		91.81
Ramachandran allowed (%)		8.19
Ramachandran outliers (%)		0.00
Rotamer outliers (%)		1.53
Clashscore		1.42
Average <i>B</i> factor (Å ²)		
Overall		33.56
Macromolecule		32.92
Cu		35.33
Cl		33.0
<i>N</i> -Acetylglucosamine		50.54
Solvent		40.84

2.3. Structure refinement

Joint X-ray/neutron refinement was performed using the *Phenix* software suite (Liebschner *et al.*, 2019) with manual model building performed in *Coot* (Emsley *et al.*, 2010).

The ligand-free model of *LsAA9_A* at pH 3.5 (PDB entry 5n04; Frandsen *et al.*, 2017) stripped of the Cu²⁺ ion and water molecules was used as the starting model. Iterative rounds of refinement and model building were conducted. When the model refined against the X-ray data alone was complete, H and D atoms were generated using the *Phenix ReadySet!* tool as described by Schröder & Meilleur (2020). The model was further refined against both the X-ray and neutron data sets. Refinement statistics are listed in Table 1.

3. Results and discussion

Neutron and X-ray data sets were collected from the same crystal to 2.8 Å and 2.1 Å resolution, respectively. The *LsAA9_A* model refined jointly against the X-ray and

neutron data includes key LPMO structural features at the active site.

3.1. Vapor exchange

Neutron diffraction data collection requires hydrogen to be exchanged for deuterium to increase the signal-to-noise ratio of the data and the visibility of the hydrogen/deuterium positions (Meilleur, 2020). Vapor exchange was performed over a period of two weeks, which is typical of the time used in a neutron protein crystallography experiment to exchange hydrogen for deuterium (O'Dell *et al.*, 2016). The hydrogen–deuterium exchange pattern for the backbone amide groups is presented in Fig. 3. As expected, the outer loops show a high level of exchange, while the inner β -sheets undergo limited exchange. However, the overall exchange is low (35%), indicating that at this low pH longer times are required to achieve higher overall exchange. The pH dependence of the amide hydrogen-exchange rate has previously been examined using mass-spectrometry experiments. These studies suggest that the exchange time required at pH 5.5 to achieve the same level of exchange as at pH 7.5 is 100 times longer (Li *et al.*, 2014). This time scale is challenging to achieve when planning for neutron data collection.

3.2. The histidine brace

As previously described for *LsAA9_A*, the Cu^{2+} ion in the joint X-ray/neutron structure presented here is coordinated by the N-terminal amino group and N^δ of His1, N^ϵ of His78 and a water molecule in the equatorial position ($\text{H}_2\text{O-eq}$), while the OH group of Tyr164 and a water molecule are located close to the axial coordination sites. The distances of the copper to the ligands are listed in Table 2.

The crystals were grown at pH 3.5. At this pH the histidine brace is disordered, with His78 adopting two conformations as reported previously for *LsAA9_A* (Frandsen *et al.*, 2017). Ordering of the histidine brace requires the pH to be increased. The pH increase is typically achieved by soaking crystals directly in buffer at pH 5.5. Here, to avoid compro-

Table 2
Distances within the *LsAA9_A* copper site.

Ligand	Copper–ligand distance (Å)
His1 N	2.2
His1 N^δ	2.0
His78 N^ϵ (0.75)/ Cl^- (0.25)†	2.1/2.5
$\text{H}_2\text{O-eq}$	2.1
$\text{H}_2\text{O-ax}$	2.7
Tyr164 O^{H}	2.8

† The occupancies of His78 and the Cl^- ligand are shown in parentheses.

mising the diffraction quality of the large crystals, the pH was increased by vapor diffusion.

Clear electron and neutron scattering-length densities were observed for His78 coordinated to Cu^{2+} , confirming that vapor pH exchange drove ordering of the histidine brace (Figs. 4*a* and 4*b*). No residual $F_o - F_c$ electron density was observed for an alternate conformation of His78 flipped away from the active-site Cu^{2+} . However, residual $F_o - F_c$ electron density indicated that a Cl^- ion from the crystallization condition alternatively coordinates the Cu^{2+} ion instead of His78 as observed in the structure of *LsAA9_A* previously solved at pH 3.5 (Frandsen *et al.*, 2017; Fig. 4*c*). The occupancies of His78 and Cl^- refined to 0.75 and 0.25, respectively. The N-terminal amino group is neutral (Fig. 4*d*).

3.3. Active-site waters

The active sites of LPMOs are readily prone to X-ray-induced photochemistry, as shown by photoreduction studies on families AA9, AA10 and AA13 (Gudmundsson *et al.*, 2014; Muderspach *et al.*, 2019; Banerjee *et al.*, 2022). At the active site of LPMO, photoreduction causes disorder (and ultimately the disappearance) of the copper-coordinating water molecules in the copper axial and equatorial positions and other geometrical changes. An advantage of neutron diffraction in the structural characterization of metalloenzymes is the lack of radiation-induced in-beam chemistry (Bodenheimer *et al.*, 2017; Schröder & Meilleur, 2021). While joint refinement

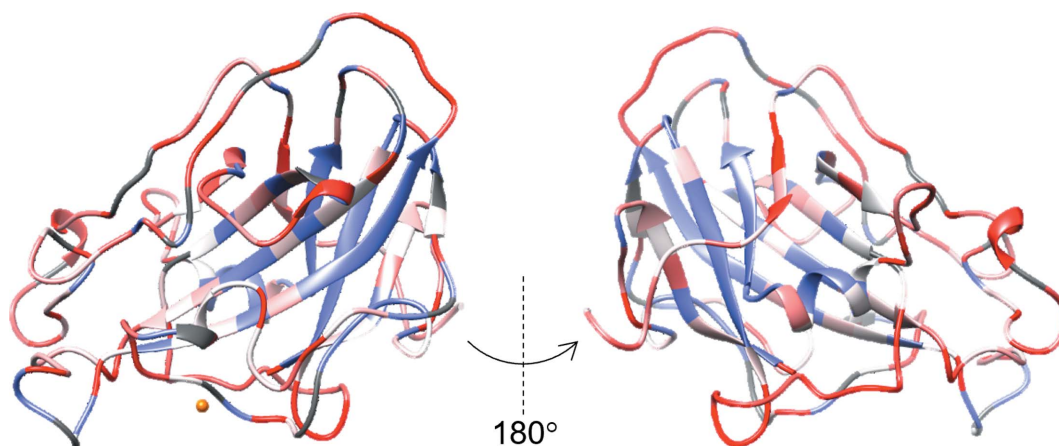


Figure 3

Hydrogen/deuterium exchange of the backbone amide groups. Full (100% D, 0% H) exchange is plotted in red. No exchange (0% D, 100% H) is plotted in blue. Copper(II) is represented by an orange sphere.

against neutron and X-ray data is a standard approach (O'Dell *et al.*, 2016), the structure refined against the X-ray data alone must be carefully examined when planning the joint X-ray/neutron refinement of a metalloenzyme. For the joint refinement performed here, we collected an X-ray data set on a home source. The X-ray data show clear $F_o - F_c$ electron-density peaks for the copper equatorial and axial water molecules, as well as for the pocket water (Fig. 5). The distances from H₂O-eq and H₂O-ax to Cu²⁺ are 2.1 and 2.7 Å, respectively, confirming that the copper ion is in the resting oxidation state, copper(II), and validating the use of the X-ray data for joint refinement (Tandrup *et al.*, 2022).

3.4. Residues near the active site: Tyr164 and His147

The LPMO family AA9 active site includes a conserved tyrosine residue. The tyrosine hydroxy group is in the second axial coordination site of the copper, but the Cu–O_{Tyr} distance is too long to form a Cu–O_{Tyr} bond. Recent analysis of X-ray structures at low X-ray dose have confirmed that on binding oligosaccharide the distance to Tyr164 is shortened (Tandrup *et al.*, 2022). In the structure presented here, Tyr164 is positioned in the axial position of the copper with a Cu–O_{Tyr} distance of 2.80 Å. The Tyr164 OH group forms a hydrogen bond to the side-chain carbonyl group of Gln162 with an O_{Tyr164}–O_{Gln162} distance of 2.72 Å. An $F_o - F_c$ nuclear map

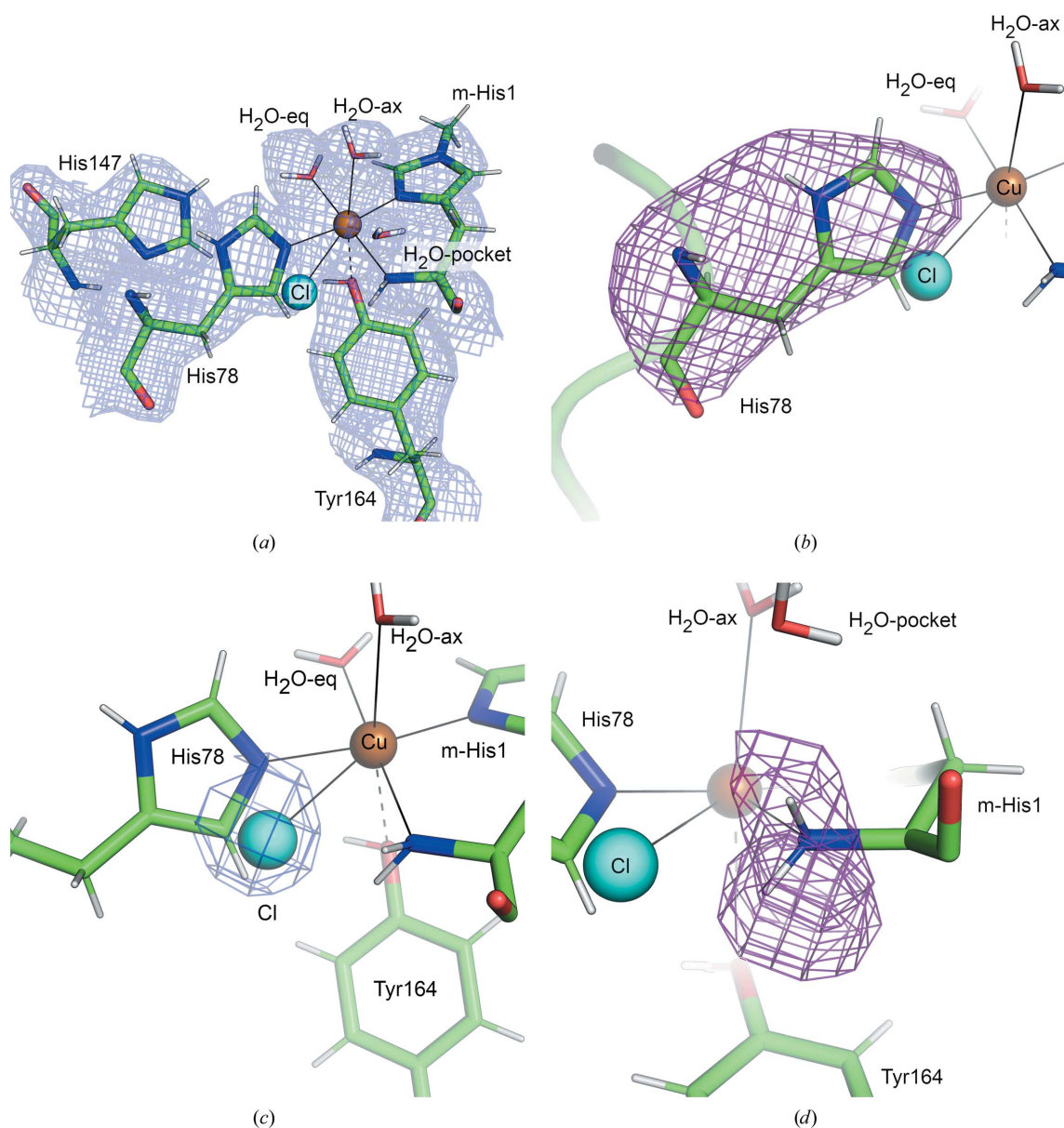


Figure 4

The *LsAA9_A* active site modeled in the joint X-ray/neutron structure at room temperature. (a) $2F_o - F_c$ electron-density map in light blue contoured at 1.0σ . (b) $F_o - F_c$ neutron scattering-length density omit map for His78 in purple contoured at 3.0σ . His78 is modeled in a single conformation with 75% occupancy. (c) $F_o - F_c$ electron-density omit map for Cl⁻ in dark blue contoured at 3.0σ . The Cl⁻ ion is modeled with 25% occupancy. (d) $F_o - F_c$ neutron scattering-length density omit map for the N-terminal amino group in purple contoured at 3.0σ , indicating that the N-terminal amino group is neutral (NH₂).

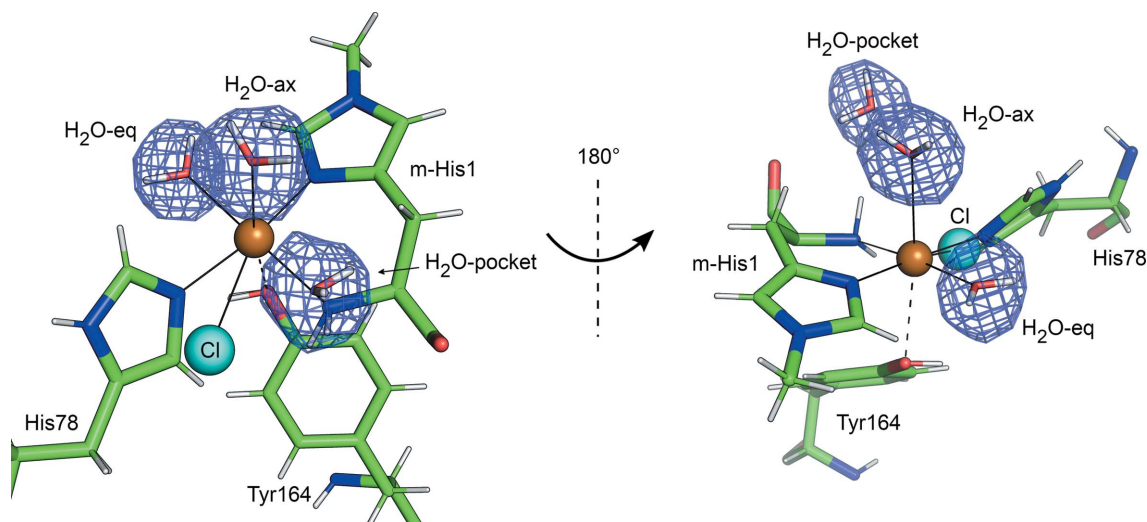


Figure 5
Active-site water molecules. $F_o - F_c$ electron-density omit map for H₂O-eq, H₂O-ax and H₂O-pocket in dark blue contoured at 7.0σ .

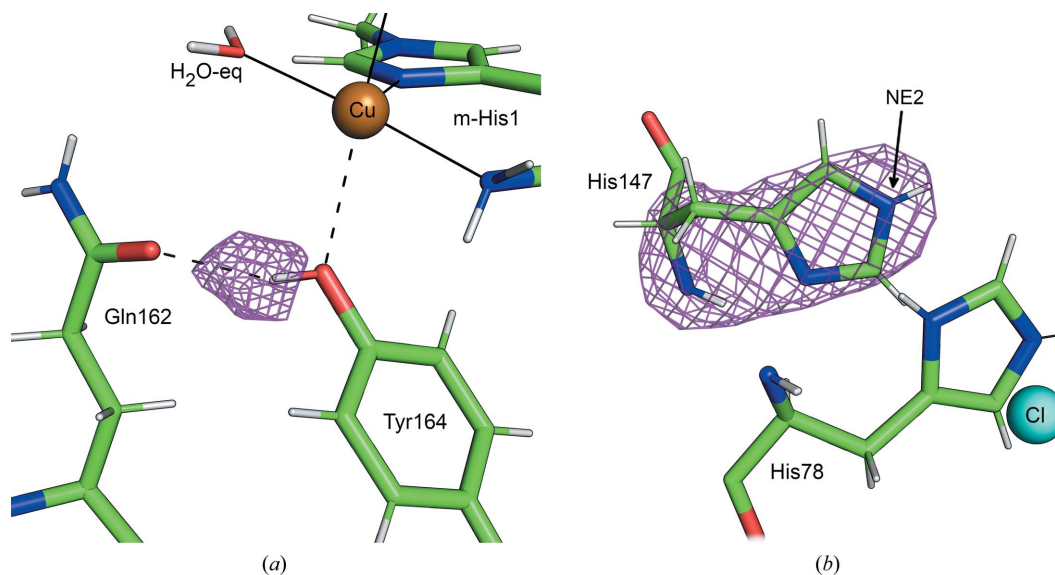


Figure 6
Conserved residues near the copper center. (a) $F_o - F_c$ neutron scattering-length density omit map for the hydroxy group of Tyr164 in purple contoured at 3.0σ . The hydrogen bond between Tyr164 and Gln162 OE1 is represented by a black dashed line. (b) $F_o - F_c$ neutron scattering-length density omit map for His147 in purple contoured at 3.0σ , indicating that His147 is singly protonated at the NE2 position.

calculated omitting the D atom of the Tyr164 hydroxy group show a clear positive peak at 3.0σ (Fig. 6a). It will be interesting to observe the effect of saccharide binding on this hydrogen bond in future neutron structures.

His147, a conserved second-shell residue, is singly protonated at the NE2 position (Fig. 6b). This confirms that in this conformation His147 remains neutral at low pH (Schröder *et al.*, 2022), as also shown by analysis of high-resolution X-ray structures (Banerjee *et al.*, 2022).

4. Conclusion

The protonation state of key amino acids in the active site of LsAA9_A could be determined despite the modest resolution

of the neutron data. For future studies, longer pH exchange times are advised, as a small amount of disorder remained at the histidine brace. Perdeuteration allows diffraction from similar-sized crystals to extend to higher resolution by eliminating the incoherent scattering of hydrogen which contributes to the high background. The heterologous expression of LsAA9_A was recently optimized in *Escherichia coli*, which opens the opportunity to perdeuterate the protein (Hernández-Rollán *et al.*, 2021). LsAA9_A produced in *E. coli* was crystallized and high-quality X-ray structures were obtained, including a complex with cellotriose (Banerjee *et al.*, 2022; Tandrup *et al.*, 2022). Future neutron structural investigation of LsAA9_A in complex with carbohydrate ligands will be greatly enhanced by the use of perdeuterated protein.

Acknowledgements

The authors thank Novozymes for expressing *LsAA9_A* in *A. oryzae* and their gift of concentrated culture medium, and Gwyndalyn Phillips for technical support. Protein purification and crystallization experiments were conducted at the Center for Structural Molecular Biology (CSMB), a US Department of Energy Biological and Environmental Research User Facility at Oak Ridge National Laboratory. Neutron diffraction data were collected on BL-11B MaNDi at the Spallation Neutron Source at ORNL, which is sponsored by the Scientific User Facilities Division, Office of Basic Energy Sciences, US Department of Energy. Thanks also to Johan Ø. Ipsen and Katja S. Johansen (University of Copenhagen) for helpful discussion and help with sample preparation.

Funding information

FM acknowledges support from USDA NIFA Hatch 211001. TT and LLL acknowledge financial support from the Novo Nordisk Foundation (HOPE project NNF17SA0027704) and the Danish Council for Independent Research (grant No. 8021-00273B). TT acknowledges the support from The Fulbright Program towards his research stay at Oak Ridge National Laboratory.

References

- Agger, J. W., Isaksen, T., Várnai, A., Vidal-Melgosa, S., Willats, W. G. T., Ludwig, R., Horn, S. J., Eijsink, V. G. H. & Westereng, B. (2014). *Proc. Natl Acad. Sci. USA*, **111**, 6287–6292.
- Arnold, O., Bilheux, J. C., Borreguero, J. M., Buts, A., Campbell, S. I., Chapon, L., Doucet, M., Draper, N., Ferraz Leal, R., Gigg, M. A., Lynch, V. E., Markvardsen, A., Mikkelsen, D. J., Mikkelsen, R. L., Miller, R., Palmen, K., Parker, P., Passos, G., Perring, T. G., Peterson, P. F., Ren, S., Reuter, M. A., Savici, A. T., Taylor, J. W., Taylor, R. J., Tolchenov, R., Zhou, W. & Zikovsky, J. (2014). *Nucl. Instrum. Methods Phys. Res. A*, **764**, 156–166.
- Arzt, S., Campbell, J. W., Hao, Q., Nguti, D., Harding, M. M., Helliwell, J. R., Bradbrook, G., Habash, J., Nieh, Y. P. & Snell, E. H. (1996). *Acta Cryst.* **A52**, C50.
- Banerjee, S., Mudderspach, S. J., Tandrup, T., Frandsen, K. E. H., Singh, R. K., Ipsen, J. O., Hernández-Rollán, C., Nørholm, M. H. H., Bjerrum, M. J., Johansen, K. S. & Lo Leggio, L. (2022). *Biomolecules*, **12**, 194.
- Berman, H. M., Westbrook, J., Feng, Z., Gilliland, G., Bhat, T. N., Weissig, H., Shindyalov, I. N. & Bourne, P. E. (2000). *Nucleic Acids Res.* **28**, 235–242.
- Bissaro, B., Røhr, Å. K., Müller, G., Chylenski, P., Skaugen, M., Forsberg, Z., Horn, S. J., Vaaje-Kolstad, G. & Eijsink, V. G. H. (2017). *Nat. Chem. Biol.* **13**, 1123–1128.
- Bodenheimer, A. M., O'Dell, W. B., Stanley, C. B. & Meilleur, F. (2017). *Carbohydr. Res.* **448**, 200–204.
- Brander, S., Tokin, R., Ipsen, J. Ø., Jensen, P. E., Hernández-Rollán, C., Nørholm, M. H. H., Lo Leggio, L., Dupree, P. & Johansen, K. S. (2021). *ACS Catal.* **11**, 13848–13859.
- Campbell, J. W., Hao, Q., Harding, M. M., Nguti, N. D. & Wilkinson, C. (1998). *J. Appl. Cryst.* **31**, 496–502.
- Coates, L. & Sullivan, B. (2020). *Methods Enzymol.* **634**, 87–99.
- Drula, E., Garron, M. L., Dogan, S., Lombard, V., Henrissat, B. & Terrapon, N. (2022). *Nucleic Acids Res.* **50**, D571–D577.
- Emsley, P., Lohkamp, B., Scott, W. G. & Cowtan, K. (2010). *Acta Cryst.* **D66**, 486–501.
- Evans, P. R. & Murshudov, G. N. (2013). *Acta Cryst.* **D69**, 1204–1214.
- Frandsen, K. E., Simmons, T. J., Dupree, P., Poulsen, J. C., Hemsworth, G. R., Ciano, L., Johnston, E. M., Tovborg, M., Johansen, K. S., von Freiesleben, P., Marmuse, L., Fort, S., Cottaz, S., Driguez, H., Henrissat, B., Lenfant, N., Tuna, F., Baldansuren, A., Davies, G. J., Lo Leggio, L. & Walton, P. H. (2016). *Nat. Chem. Biol.* **12**, 298–303.
- Frandsen, K. E. H., Poulsen, J. N., Tandrup, T. & Lo Leggio, L. (2017). *Carbohydr. Res.* **448**, 187–190.
- Gudmundsson, M., Kim, S., Wu, M., Ishida, T., Momeni, M. H., Vaaje-Kolstad, G., Lundberg, D., Royant, A., Ståhlberg, J., Eijsink, V. G. H., Beckham, G. T. & Sandgren, M. (2014). *J. Biol. Chem.* **289**, 18782–18792.
- Helliwell, J. R., Habash, J., Cruickshank, D. W. J., Harding, M. M., Greenhough, T. J., Campbell, J. W., Clifton, I. J., Elder, M., Machin, P. A., Papiz, M. Z. & Zurek, S. (1989). *J. Appl. Cryst.* **22**, 483–497.
- Hernández-Rollán, C., Falkenberg, K. B., Rennig, M., Bertelsen, A. B., Ipsen, J. Ø., Brander, S., Daley, D. O., Johansen, K. S. & Nørholm, M. H. H. (2021). *ACS Synth. Biol.* **10**, 897–906.
- Johansen, K. S. (2016). *Biochem. Soc. Trans.* **44**, 143–149.
- Levasseur, A., Drula, E., Lombard, V., Coutinho, P. M. & Henrissat, B. (2013). *Biotechnol. Biofuels*, **6**, 41.
- Li, J., Rodnin, M. V., Ladokhin, A. S. & Gross, M. L. (2014). *Biochemistry*, **53**, 6849–6856.
- Liebschner, D., Afonine, P. V., Baker, M. L., Bunkóczi, G., Chen, V. B., Croll, T. I., Hintze, B., Hung, L.-W., Jain, S., McCoy, A. J., Moriarty, N. W., Oeffner, R. D., Poon, B. K., Prisant, M. G., Read, R. J., Richardson, J. S., Richardson, D. C., Sammito, M. D., Sobolev, O. V., Stockwell, D. H., Terwilliger, T. C., Urzhumtsev, A. G., Videau, L. L., Williams, C. J. & Adams, P. D. (2019). *Acta Cryst.* **D75**, 861–877.
- Meilleur, F. (2020). *Biochemist*, **42**, 16–20.
- Meilleur, F., Coates, L., Cuneo, M. J., Kovalevsky, A. & Myles, D. A. F. (2018). *Crystals*, **8**, 388.
- Mudderspach, S. J., Tandrup, T., Frandsen, K. E. H., Santoni, G., Poulsen, J.-C. N. & Lo Leggio, L. (2019). *Amylase*, **3**, 41–54.
- O'Dell, W. B., Agarwal, P. K. & Meilleur, F. (2017). *Angew. Chem. Int. Ed.* **56**, 767–770.
- O'Dell, W. B., Bodenheimer, A. M. & Meilleur, F. (2016). *Arch. Biochem. Biophys.* **602**, 48–60.
- O'Dell, W. B., Swartz, P. D., Weiss, K. L. & Meilleur, F. (2017). *Acta Cryst.* **F73**, 70–78.
- Schröder, G. C. & Meilleur, F. (2020). *J. Vis. Exp.*, e61903.
- Schröder, G. C. & Meilleur, F. (2021). *Acta Cryst.* **D77**, 1251–1269.
- Schröder, G. C., O'Dell, W. B., Myles, D. A. F., Kovalevsky, A. & Meilleur, F. (2018). *Acta Cryst.* **D74**, 778–786.
- Schröder, G. C., O'Dell, W. B., Swartz, P. D. & Meilleur, F. (2021). *Acta Cryst.* **F77**, 128–133.
- Schröder, G. C., O'Dell, W. B., Webb, S. P., Agarwal, P. K. & Meilleur, F. (2022). *Chem. Sci.* **13**, 13303–13320.
- Simmons, T. J., Frandsen, K. E. H., Ciano, L., Tryfona, T., Lenfant, N., Poulsen, J. C., Wilson, L. F. L., Tandrup, T., Tovborg, M., Schnorr, K., Johansen, K. S., Henrissat, B., Walton, P. H., Lo Leggio, L. & Dupree, P. (2017). *Nat. Commun.* **8**, 1064.
- Sullivan, B., Archibald, R., Langan, P. S., Dobbek, H., Bommer, M., McFeeters, R. L., Coates, L., Wang, X. P., Gallmeier, F., Carpenter, J. M., Lynch, V. & Langan, P. (2018). *Acta Cryst.* **D74**, 1085–1095.
- Tandrup, T., Mudderspach, S. J., Banerjee, S., Santoni, G., Ipsen, J. Ø., Hernández-Rollán, C., Nørholm, M. H. H., Johansen, K. S., Meilleur, F. & Lo Leggio, L. (2022). *IUCrJ*, **9**, 666–681.
- Tandrup, T., Tryfona, T., Frandsen, K. E. H., Johansen, K. S., Dupree, P. & Lo Leggio, L. (2020). *Biochemistry*, **59**, 3347–3358.
- Vandhana, T. M., Reyre, J. L., Sushmaa, D., Berrin, J. G., Bissaro, B. & Madhuprakash, J. (2022). *New Phytol.* **233**, 2380–2396.
- Winn, M. D., Ballard, C. C., Cowtan, K. D., Dodson, E. J., Emsley, P., Evans, P. R., Keegan, R. M., Krissinel, E. B., Leslie, A. G. W., McCoy, A., McNicholas, S. J., Murshudov, G. N., Pannu, N. S., Potterton, E. A., Powell, H. R., Read, R. J., Vagin, A. & Wilson, K. S. (2011). *Acta Cryst.* **D67**, 235–242.